Available online at www.sciencedirect.com

ScienceDirect

IFAC PapersOnline CONFERENCE PAPER ARCHIVE

IFAC PapersOnLine 54-8 (2021) 124–129

Finite Horizon Touchdown Analysis of Autolanded Aircraft under Crosswind

Felix Biertümpfel * **Harald Pfifer** *

* *Technische Universität Dresden, Institute of Aerospace Systems, Chair of Flight Mechanics and Control, 01307 Dresden, Germany (e-mail: felix.biertuempfel@tu-dresden.de, harald.pfifer@tu-dresden.de)*

Abstract: The paper presents a worst-case touchdown condition analysis of an autolanded aircraft under crosswind. Aircraft dynamics are generally considered altitude- and speed-dependent and, thus, well covered inside the linear parameter-varying framework. Following a specific parameter trajectory tracking the instrument landing system's guidance signal, its dynamics amount to a finite horizon linear time-varying (LTV) system. This allows to explicitly respect the varying dynamics during the flare maneuver, changing control laws, and the finite horizon of the approach using a finite horizon LTV analysis. A time-varying trajectory uncertainty is proposed to respect the effects of different environmental conditions and aircraft parameters in the analysis. By representing the uncertainty as an integral quadratic constraint (IQC), recent advances in the worst-case gain analysis of finite horizon LTV systems can be utilized. The analysis condition is based on a parameterized Riccati differential equation, which leads to an efficiently solvable nonlinear optimization problem. Applying the robust LTV framework, worst-case touchdown conditions of an autolanded large airliner under crosswind wind are calculated. The obtained results are evaluated against Monte Carlo analyses of the nonlinear model.

Keywords: Robust Control, Linear Time-Varying Systems, Integral Quadratic Constraints, Aircraft Control, Aerospace Applications

1. INTRODUCTION

The final approach of an aircraft is the most hazardous flight phase accounting for more than 49% of all recorded fatal accidents, see Boeing (2018). Autoland systems were introduced to mitigate the risk, especially for poor visual conditions in the early 1950s (Birkle (1956)). These commonly use a runway-based instrument landing system (ILS) to provide a localizer and glide slope signal tracked by the aircraft's autopilot. Given its operational range, the autoland system must fulfill rigorous touchdown constraints for safe operation.

The state-of-the-art approaches to evaluate touchdown conditions and constraints are Monte Carlo analyses (Biannic and Roos (2015)) or worst case optimizations conducted on the nonlinear model (Misra and Bai (2020)). Due to the large parameter space of the aircraft, the variety of environmental conditions, and disturbances, these procedures are computationally expensive. Hence, they are not suitable to provide fast feedback in an iterative design/tuning process of the autopilot. Furthermore, they cannot provide actual worst-cases, but only a probability distribution or a lower bound of the worst-case, respectively.

A common approach for worst-case analysis of aircraft dynamics exists in the form of the linear parameter-varying (LPV) framework. An example of a worst-case analysis method for LPV systems based on integral quadratic constraints (IQCs) is, for example, given in Pfifer and Seiler (2016). It is suitable to efficiently analyze various design constraints such as gust loads (Knoblach et al. (2015)). A single LPV analysis covers an infinite amount of admissible trajectories in the parameter set over infinite time horizons. However, during the (automated) final approach, the aircraft only follows one specific trajectory in this set by tracking the ILS signals. Consequently, the dynamics can be treated as solely time-dependent over a finite horizon, i.e. as a linear-time varying system (LTV), which is a special form of LPV systems. Treating the aircraft as a finite horizon LTV system allows applying the robust LTV bounded real lemma (BRL), which is an extension of the IQC based LPV framework for worst-case analysis, see e.g. Seiler et al. (2019) or Biertümpfel and Pfifer (2018). The latter provides an efficient approach to analyze uncertain LTV systems over long time horizons. It was shown feasible in an industry-relevant worst-case loads analysis of a space launcher (Biertümpfel and Pfifer (2019)).

This paper proposes a robust LTV worst-case analysis for lateral touchdown conditions of an autolanded aircraft under crosswind. The nonlinear aircraft dynamics are directly taken from Biannic and Boada-Bauxell (2017), which provides an A330-like aircraft model in final approach configuration with the corresponding nonlinear simulation environment. It is freely available from *http://w3.onera.fr/smac/?q=aircraftModel* and briefly described in Section 3.1. The LTV representation of the aircraft dynamics is derived by numerical linearization along a reference trajectory, described in Section 3.3. An autoland controller for this aircraft model has been developed in Theis et al. (2018) and is analyzed in this paper in Section 4.

To cover realistic wind disturbance under the constraints of the strict BRL, a tailored wind filter is designed. It shapes an arbitrary norm-bounded input signal into a wind disturbance whose PSD is comparable to Dryden-like turbulence commonly used in nonlinear analysis. Additionally, the influence of altitude-dependent wind fields, e.g. wind shears, is implicitly covered in the aircraft's linearized dynamics. The LTV worst-case analysis

10.1016/j.ifacol.2021.08.591

results are compared to a Monte Carlo analysis conducted on the corresponding high-fidelity nonlinear aircraft model.

2. BACKGROUND ON LTV ROBUSTNESS ANALYSIS

2.1 Linear Time-Varying Systems

A finite horizon continuous LTV system G_t is a special case of LPV system, which is limited to a single trajectory. It is defined as

$$\begin{aligned} \dot{x}_t(t) &= A_t(t)\, x_t(t) + B_t(t)\, d(t) \\ e(t) &= C_t(t)\, x_t(t) + D_t(t)\, d(t), \end{aligned} \tag{1}$$

where $x_t(t) \in \mathbb{R}^{n_{x_t}}$ denotes the state vector, $d(t) \in \mathbb{R}^{n_d}$ the input vector, and $e(t) \in \mathbb{R}^{n_e}$ the output vector. The system matrices of an LTV system are locally bounded continuous functions of time t with compatible size to the corresponding vectors, e.g. $A_t(t) \in \mathbb{R}^{n_{x_t} \times n_{x_t}}$. The explicit time dependency will be omitted regularly to shorten the notation. In this paper, the size of a signal $d(t)$ will be described by the finite horizon Lebesgue 2-norm:

$$\|d\|_{2[0,T]} = \sqrt{\int_0^T d^T(t) d(t)\, dt} \tag{2}$$

as defined in Tadmor (1990).

2.2 Integral Quadratic Constraints

IQCs are used to bound the input/output behavior of an uncertainty Δ. The time-domain definition of an IQC is based on a filter $\Psi \in \mathbb{RH}_\infty^{n_z \times (n_v + n_w)}$ and a $n_z \times n_z$ real, symmetric matrix $M \in \mathbb{S}^{n_z \times n_z}$ (Seiler (2015)). The graphical representation of a time domain IQC is shown in Fig. 1. The uncertainty Δ satisfies

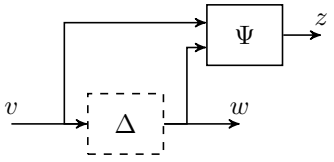

Fig. 1. Feedback Interconnection LTV system G_t and uncertainty Δ

the IQC defined by M and Ψ if the output z of the filter Ψ fulfills the quadratic time constraint

$$\int_0^T z(t)^T M z(t)\, dt \geq 0 \tag{3}$$

for all $v \in L_2[0,T]$ and $w = \Delta(v)$ over the interval $[0,T]$. In this case, the short notation $\Delta \in IQC(\Psi, M)$ is used.

2.3 Robust LTV Performance Analysis

A robust performance analysis framework, see e.g. Biertümpfel and Pfifer (2018) or Seiler et al. (2019) for details, can be derived from the worst-case analysis condition of nominal LTV systems in Green and Limebeer (1995). The framework covers the feedback interconnection $F_u(G_t, \Delta)$ of a known LTV system G_t and a perturbation Δ. It is assumed that the perturbation Δ satisfies an IQC described by Ψ and M, i.e. $\Delta \in IQC(\Psi, M)$. Consequently, the feedback interconnection can be extended by the IQC filter Ψ as depicted in Fig. 2. The extension leads to the extended LTV system G, whose

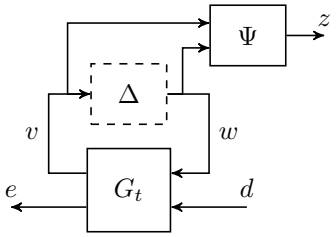

Fig. 2. Feedback Interconnection LTV system G_t and uncertainty Δ

dynamics are described by

$$\begin{aligned} \dot{x}(t) &= A(t)\, x(t) + \begin{bmatrix} B_1(t) & B_2(t) \end{bmatrix} \begin{bmatrix} w(t) \\ d(t) \end{bmatrix} \\ \begin{bmatrix} z(t) \\ e(t) \end{bmatrix} &= \begin{bmatrix} C_1(t) \\ C_2(t) \end{bmatrix} x(t) + \begin{bmatrix} D_{11}(t) & D_{12}(t) \\ D_{21}(t) & D_{22}(t) \end{bmatrix} \begin{bmatrix} w(t) \\ d(t) \end{bmatrix}, \end{aligned} \tag{4}$$

where $x(t) \in \mathbb{R}^{n_x}$ is the state vector of the combined systems G_t and Ψ, $d(t) \in \mathbb{R}^{n_d}$ the input vector, and $e(t) \in \mathbb{R}^{n_e}$ the output vector. The time-domain inequality (3) enforced on the output z of Ψ is used to replace the explicit representation of the uncertainty $w = \Delta(v)$.

For the interconnection depicted in Fig. 2, the finite horizon worst case $L_2[0,T]$ to $\|e(T)\|_2$ gain is defined as:

$$\|F_u(G_t, \Delta)\|_2 := \sup_{\Delta \in \mathrm{IQC}(\Psi, M)} \sup_{\substack{d \in L_2[0,T] \\ d \neq 0, x(0)=0}} \frac{\|e(T)\|_2}{\|d(t)\|_{2[0,T]}}. \tag{5}$$

Geometrically interpreted, it describes the ball upper bounding the worst-case output $e(T)$ at the terminal time T over all $\Delta \in IQC(\Psi, M)$ for $\|d(t)\|_{2[0,T]} \leq 1$.

Using the extended system G (4) and the time-domain IQC formulation (3), a dissipation inequality can be derived providing an upper bound on the worst-case $L_2[0,T]$ to $\|e(T)\|_2$ gain of the interconnection $F_u(G_t, \Delta)$ (Seiler et al. (2019); Biertümpfel and Pfifer (2018)). This dissipation inequality leads to a linear matrix inequality, which can be expressed as an equivalent condition based on the integrability of a Riccati differential equation (RDE). The latter is provided in the following theorem.

Theorem 1. Let $F_u(G_t, \Delta)$ be well posed $\forall\, \Delta \in IQC(\Psi, M)$, then $\|F_u(G_t, \Delta)\|_2 < \gamma$ if there exists a continuously differentiable symmetric $P : [0,T] \to \mathbb{R}^{n_x \times n_x}$ such that

$$P(T) = \frac{1}{\gamma} C_2(T)^T C_2(T), \tag{6}$$

$$\dot{P} = Q + P\tilde{A} + \tilde{A}^T P - PSP \qquad \forall t \in [0,T], \tag{7}$$

and

$$R = \begin{bmatrix} D_{11}^T M D_{11} & D_{11}^T M D_{12} \\ D_{12}^T M D_{11} & D_{12}^T M D_{12} - \gamma I \end{bmatrix} < 0 \,\forall\, t \in [0,T], \tag{8}$$

with

$$\tilde{A} = \begin{bmatrix} B_1 & B_2 \end{bmatrix} R^{-1} \begin{bmatrix} (C_1^T M D_{11})^T \\ (C_1^T M D_{12})^T \end{bmatrix} - A, \tag{9}$$

$$S = -\begin{bmatrix} B_1 & B_2 \end{bmatrix} R^{-1} \begin{bmatrix} B_1^T \\ B_2^T \end{bmatrix} \tag{10}$$

and

$$\begin{aligned} Q = &-C_1^T M C_1 \\ &+ \begin{bmatrix} (C_1^T M D_{11})^T \\ (C_1^T M D_{12})^T \end{bmatrix}^T R^{-1} \begin{bmatrix} (C_1^T M D_{11})^T \\ (C_1^T M D_{12})^T \end{bmatrix}. \end{aligned} \tag{11}$$

Proof. The proof is based on the definition of a time-dependent quadratic storage function $V(x,t) = x^T P(t) x$. After perturbing (7), the resulting Riccati differential inequality can be rewritten as an LMI applying the Schur complement. Multiplying $[x^T, w^T, d^T]$ and $[x^T, w^T, d^T]^T$ on the left and right

side respectively of the LMI results in a dissipation inequality. Integration from 0 to T for zero initial conditions gives

$$\int_0^T z(t)^T M z(t) dt - \gamma \int_0^T d(t)^T d(t) dt + x(T)^T P(T) x(T) < 0. \tag{12}$$

Equality (6) is perturbed and left and right multiplied with $x(T)^T$ and $x(T)$ respectively resulting in

$$x(T)^T P(T) x(T) - \frac{1}{\gamma} e(T)^T e(T) = 0. \tag{13}$$

Substituting (13) in (12) and applying the vector 2-norm (Euclidean) $\|e(T)\|_2^2 = e(T)^T e(T)$ results in the upper bound on (5) given by γ. ■

Note that a detailed proof can be found in Seiler et al. (2019).

2.4 Computational Approach

Generally, a given Δ can be described by an infinite amount of IQCs. The standard approach found in literature, see e.g. Pfifer and Seiler (2016) or Veenman et al. (2016), is to select a fixed filter Ψ and freely parameterize M. Thus, M lies within a feasibility set $\mathcal{M}$ such that $\Delta \in IQC(\Psi, M)$ for all $M \in \mathcal{M}$. Given this approach, Theorem 1 describes a parameterized RDE. A feasible parametrization for a full-block uncertain LTI dynamic can be found in Veenman et al. (2016), which will be used in the course of this paper.

Example 1. Let Δ be a full-block dynamic LTI uncertainty, with $\Delta \in \mathbb{RH}_\infty^{n_w \times n_v}$ and $0 < \|\Delta\|_\infty \leq b$. A valid time domain IQC for Δ is defined by $\Psi = \left[\begin{smallmatrix} b\psi_\nu \otimes I_{n_v} & 0 \\ 0 & \psi_\nu \otimes I_{n_w} \end{smallmatrix}\right]$ and $\mathcal{M} := \{M = \left[\begin{smallmatrix} X \otimes I_{n_v} & 0 \\ 0 & -X \otimes I_{n_w} \end{smallmatrix}\right] : X = X^T \geq 0 \in \mathbb{R}^{(\nu+1)\times(\nu+1)}\}$. A typical choice for $\psi_\nu \in \mathbb{RH}_\infty^{(\nu+1)\times 1}$ is:

$$\psi_\nu = \left[1 \;\; \tfrac{1}{(s-\rho)} \;\; \dots \;\; \tfrac{1}{(s-\rho)^\nu}\right]^T, \; \rho < 0 \,, \; \nu \in \mathbb{N}_0. \tag{14}$$

In the optimization, ψ_ν is a fixed basis function with preselected ν and ρ, whereas X is a free optimization parameter. This leads to a nonlinear optimization problem to minimize the upper bound γ on the worst-case gain:

$$\begin{aligned} &\min_{M \in \mathcal{M}} \gamma \\ &\text{such that } \forall t \in [0, T] \\ &\qquad P(T) = \frac{1}{\gamma} C_2(T)^T C_2(T) \\ &\qquad \dot{P} = Q + P\tilde{A} + \tilde{A}^T P - PSP \\ &\qquad R < 0 \end{aligned} \tag{15}$$

In Biertümpfel and Pfifer (2018), an algorithm to efficiently solve the optimization problem is given. It essentially performs a bisection of γ for a fixed M in an inner loop. The outer loop applies a global optimization to identify the optimal parameterization $M \in \mathcal{M}$ and minimal γ.

3. AUTOLANDING MODEL

3.1 Nonlinear Dynamics

The nonlinear aircraft model represents a large twin-engine civil transport aircraft in landing configuration from 1000ft above the runway until touchdown and is taken from Biannic and Boada-Bauxell (2017). It is modeled as a standard nonlinear six-degrees-of-freedom flight mechanics model with translational velocities u, v, and w, as well as the angular velocities around the roll (p), pitch (q), and yaw (r) axis in the body-fixed frame. The aircraft's orientation with respect to the earth-fixed reference frame is described by the standard Euler angles Φ, Θ, and Ψ, see e.g. McRuer et al. (1974). The position of the aircraft's center of gravity in the earth fixed frame is described by x, y, and z. The flight path with respect to earth is defined by the path angle γ, course angle χ, and ground speed V_g, i.e. the horizontal speed relative to the earth's surface. Based on the aerodynamic velocity, which results from superimposing the aircraft's translational velocity and wind, the aerodynamic angle of attack α and sideslip angle β are defined. The aircraft's aerodynamics include the ground effect. During the approach, the aircraft is controlled by two anti-symmetrically operating ailerons (δ_a), an elevator (δ_e), a rudder (δ_e), and symmetrically operating twin engines. Finally, an atmospheric model based on the International Standard Atmosphere is included.

3.2 Autolanding Controller

In this paper, the autoland controller developed in Theis et al. (2018) is analyzed. Its design considers the lateral and longitudinal motion as decoupled. The presented analysis is limited to the lateral motion of the aircraft. Therefore, only the lateral control system is described as depicted in Fig. 3.

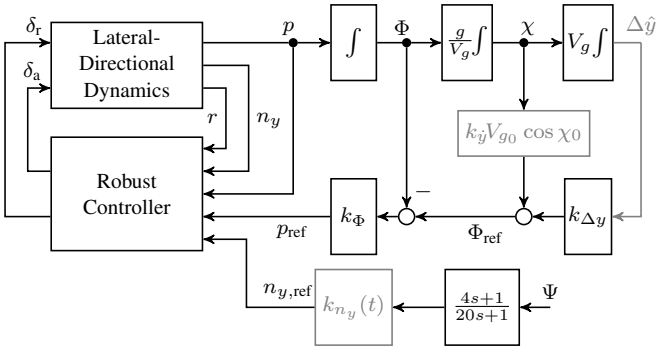

Fig. 3. Lateral part of the autoland controller as used in the LTV analysis (adaptations highlighted)

The *Robust Controller* block represents a ninth-order multivariable H_∞ controller. It provides lateral directional control via roll rate and lateral load factor feedback, damping augmentation of the dutch-roll mode via yaw rate feedback, and adverse yaw cancellation via a pronounced roll rate to rudder forward-feed. Furthermore, it adds lead compensation and roll-off characteristics.

The reference roll rate for the inner loop controller is provided by the bank angle tracking realized by proportional bank angle feedback. It is implemented as

$$p_\mathrm{ref} = k_\phi \left(\phi_\mathrm{ref} - \phi\right), \tag{16}$$

with $k_\phi = 0.7$.

The reference bank angle in (16) is provided by the localizer tracker implemented as proportional-derivative (PD) controller. Rather than directly implementing a differentiator, $\Delta\dot{y}$ is approximated by $\Delta\dot{y} \approx V_g \sin\chi$. Thus, the controller is implemented as

$$\phi_\mathrm{ref} = k_{\Delta y} \Delta\hat{y} + k_{\dot{y}} V_g \sin\chi, \tag{17}$$

with $k_{\Delta y} = 0.003$ and $k_{\dot{y}} = 0.033$. The signal $\Delta\hat{y}$ measures the actual landing gear offset to the centerline rather than the sensor's offset to the centerline Δy.

The decrab maneuver is initiated at a fixed height above ground level H_{AGL} of 5m. Following a specific trajectory, this altitude maps to a time t_{DC}. The model uses a ψ feedback controller with lag compensator given by

$$n_{y,\text{ref}} = k_{n_y} \frac{4s+1}{20s+1}\psi, \tag{18}$$

with $k_{n_y} = 33$ after initiation of the decrab maneuver and zero before.

3.3 Linear Dynamics

The LTV representation of the aircraft is derived by linearizing the nonlinear model along a nominal approach trajectory. This trajectory is calculated based on a reference autoland approach in the nonlinear simulation. For the nominal aircraft configuration, a center of gravity position of 22% and a mass of 140t are chosen. The respective airfield is on mean sea level given nominal ISA conditions. The simulation starts at an altitude of 300m, 30m below the glide slope signal, and 20m right of the localizer signal and ends with the aircraft's touchdown. The lateral nonlinear aircraft dynamics are linearized using the tools provided by Biannic and Boada-Bauxell (2017). This results in a finite horizon LTV representation G_t of the aircraft's dynamics. In interconnection with the autoland controller, the resulting closed-loop, as pictured in Fig. 3, has a total of 19 states, and three performance outputs, namely bank angle ϕ, lateral offset to the centerline y_{LG}, and the landing gear's sideslip angle relative to the centerline β_{LG}. The single disturbance input is the lateral turbulence v_w. Note that the influence of a static wind profile can be implicitly respected in the LTV dynamics by including it in the calculation of the reference trajectory, i.e. executing the reference approach with a static wind field.

3.4 Wind Model

The wind disturbance analyzed in this paper is derived from Biannic and Boada-Bauxell (2017). Theis et al. (2018) also used it for the design verification of the autoland controller. It is built by the superposition of an altitude dependent wind shear and a turbulent wind field. The touchdown conditions are analyzed for two distinct wind scenarios. First a tailwind with a fixed maximum amplitude of 10kts is analyzed. The second analysis covers headwind with a fixed maximum amplitude of 30kts. In both scenarios, simultaneously, a lateral wind shear superimposed with turbulent crosswind is applied. The lateral wind shear has a fixed maximum amplitude of 25kts. Its amplitude is inverse-proportional to the altitude and reaches its maximum 15m above ground as described by

$$v_{\text{lat}} = 25\text{kts} \cdot \min\left(\frac{(H_{\text{AGL}} - H_{\text{AGL},0})^2}{(H_{\text{AGL},0} - 15\text{m})^2}, 1\right), \tag{19}$$

where $H_{\text{AGL},0}$ is the altitude at initialization of the analysis. The turbulence is generated by filtering a random number signal with a mean of zero, variance of one, and sample time of 0.05s through the first-order filter G_{lat}:

$$G_{\text{lat}} = \sigma_{\text{lat}} \frac{20}{2.5s+1}. \tag{20}$$

The turbulence intensity σ_{lat} has a fixed value of 5.8kts. Note that the head- and tailwind profiles are shaped equivalent to the lateral wind shear, using the relation (19).

Due to their altitude dependence, the wind shear profiles are unique for a specific trajectory. Thus, calculating the reference trajectory under the respective wind scenario, the derived linear model includes the wind profiles influence on the aircraft dynamics. Hence, only the turbulent component must be covered in the LTV analysis.

As the turbulence filter (20) requires a white noise input, it cannot be directly applied in the LTV analysis. Recalling the definition of the $L_2[0,T]$ to $\|e(T)\|_2$ gain, the LTV wind filter has to be designed in such a way that it converts any $L_2[0,T]$ bounded signal into realistic turbulence. In particular, the LTV wind filter's design goal is to match the power spectral density (PSD) of the turbulence signals in the nonlinear simulation.

The proposed design procedure consists of four steps. In the first step, 2000 random turbulence profiles are generated along the nominal approach trajectory using the nonlinear simulation's turbulence wind model with a fixed sampling of 20Hz. The second step is to calculate the PSDs $\Omega_{v_{w,i}}$ of the time domain wind signals $v_{w,i}(t)$ using

$$\Omega_{v_{w,i}}(\omega) = \lim_{T\to\infty} \frac{1}{\pi}\frac{1}{T}\left|\int_{-T}^{T} v_{w,i}(t)e^{-j\omega t}dt\right|^2. \tag{21}$$

The PSD of a time-domain signal is simply the average squared of the signal's Fourier transform. The Fourier transform of the wind signals can be calculated via a fast Fourier transform (FFT), e.g. using the built-in Matlab function `fft`. In the third step, a minimum phase first order transfer function is calculated, upper bounding the calculated $\sqrt{|\Omega_{v_{w,i}}(\omega)|}$ of all wind signals using the built-in Matlab function `fitmagfrd`. Subsequently, the transfer function is transformed into a state-space representation of the wind filter $G_{\text{lat,LTV}}$. In the fourth step, it is checked if the derived wind filter produces adequate wind disturbance signals. The nominal LTV aircraft model closed loop is extended with $G_{\text{lat,LTV}}$. Subsequently, the nominal LTV worst-case disturbance signal d_{WC} is calculated using the procedure in Iannelli et al. (2019). Filtering d_{WC} through $G_{\text{lat,LTV}}$ provides the corresponding worst-case wind signal. In case the LTV wind signals underestimate the amplitude of the underlying turbulence, steps three and four are repeated with an increased lower bound for `fitmagfrd` until the amplitudes show an adequate match. In combination, steps three and four assure matching PSDs of the LTV worst-case wind signal and the nonlinear model's turbulence. In Fig. 4 the PSDs of the nominal worst-case LTV wind signal for the lateral displacement due to lateral turbulence is compared to the PSD of lateral turbulence profiles used in the Monte Carlo Simulation.

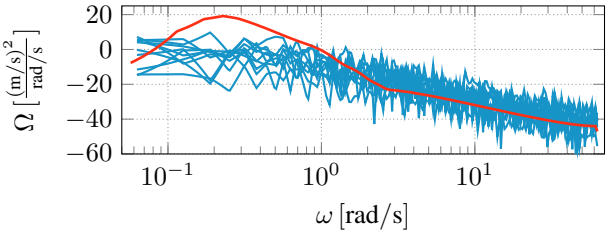

Fig. 4. Comparison of the PSD of the nominal worst case disturbance LTV signal (v_w to y_{LG}) and turbulence to generate the wind filter: LTV (——), Monte Carlo (——)

Table 1. Aircraft and environmental parameters covered in Monte Carlo Analysis

Parameter	Distribution*	min	max
Mass $[t]$	uniform	120	180
Center of mass [%]	uniform	15	41
Temperature $[°C]$	uniform	-69	40
Runway slope [%]	$\mathcal{N}(0, 0.4)$	-2	2
Glide Slope [°]	$\mathcal{N}(-3, 0.075)$	-3.15	-2.85
Runway elevation [ft]	$[-1000, 250] : 50\%$	-1000	9200
	$[250, 750] : 28.33\%$		
	$[750, 1250] : 13.33\%$		
	$[1250, 1750] : 3.33\%$		
	$[1750, 2500] : 1.67\%$		
	$[2500, 3500] : 1.00\%$		
	$[3500, 4500] : 0.67\%$		
	$[4500, 9200] : 1.67\%$		

*$\mathcal{N}(\mu, \sigma)$: normal distribution with mean μ and standard deviation σ.

3.5 Uncertainty Model

The LTV analysis must cover the aircraft configurations and environmental conditions evaluated in the Monte Carlo analysis, as summarized in Tab. 1. As different aircraft and environmental parameters directly influence the aircraft's dynamics and the approach trajectory, the corresponding LTV closed-loop dynamics differ from the nominal configuration in Section 3.3. Explicitly respecting every uncertain parameter in Tab. 1 results in an extensive IQC parameterization. Therefore, the following uncertain LTV representation of the lateral closed loop is introduced, whose range of behaviors covers the dynamics of a large set of approaches:

$$G_{\text{CL}} = G_{\text{CL,nom}}(1 + W_t\Delta). \tag{22}$$

In (22), Δ is a norm bounded dynamic LTI uncertainty, with $\|\Delta\|_\infty \leq 1$ and W_t is a time varying shaping filter. A weighting filter W_t is calculated based on Hindi et al. (2002). Firstly, LTV models resulting from 200 approaches are generated using parameter combinations based on Tab. 1 and the static wind profile (19). At frozen altitudes, the time-invariant weighting W is calculated such that all derived approach models are included in the uncertainty set (22). Afterward, the altitude grid is mapped back to the time grid of the nominal approach trajectory resulting in a time-dependent grid of weights. Finally, the time-varying weighting filter W_t is obtained by piecewise cubic polynomial interpolation of the obtained weights over the time grid of the nominal trajectory. Note that a separate weighting filter must be calculated for the head and tailwind analysis with simultaneous lateral wind shear as described in Section 3.4.

4. ANALYSIS

4.1 Analysis Setup

The general analysis interconnection for the LTV analyses is shown in Fig. 5. It is used to evaluate three performance criteria, namely bank angle ϕ, lateral offset to the centerline y_{LG}, and the landing gear's sideslip angle relative to the centerline β_{LG}, at touchdown. These are represented by e in Fig. 5. The signal y_{m} describes the controller inputs from Fig 3. Two wind scenarios as described in Section 3.4 are analyzed. Thus, the blocks C and $G_{\text{A/C}}$ represent the LTV models of the autoland controller and the aircraft dynamics, respectively. They are both derived for similar lateral wind shears, but either 30kts headwind or 10kts tailwind. The block W_t is the corresponding time-varying weight, and Δ represents the dynamic LTI uncertainty.

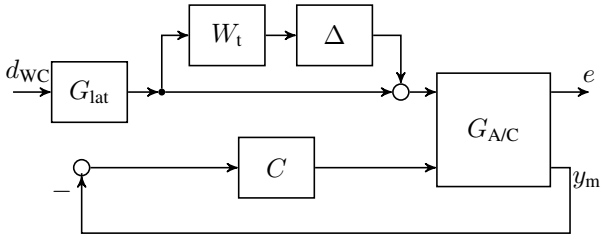

Fig. 5. Lateral LTV worst-case analysis interconnection

The LTV worst-case touchdown conditions are calculated applying the algorithm in Biertümpfel and Pfifer (2018) on the nonlinear optimization problem (15). Therefore, the interconnection in Fig. 5 must be transferred into the LTV robustness analysis framework described in Section 2. The IQC described in Example 1 is used to cover the behavior of the uncertainty Δ. In this specific case, $n_v = n_w = 1$ and the IQC factorization is defined by $\nu = 1$ and $\rho = -0.75$. Hence, $\Delta \in IQC(\Psi, M)$, with M restricted to the set $\mathcal{M} := \{M = \left[\begin{smallmatrix} X & 0 \\ 0 & -X \end{smallmatrix}\right] : X = X^T \geq 0 \in \mathbb{R}^{2\times 2}\}$ and $\Psi = \left[\begin{smallmatrix} \psi_1 & 0 \\ 0 & \psi_1 \end{smallmatrix}\right]$. The finite horizon worst-case $L_2[0, T]$ to Euclidean gain only bounds the Euclidian vector norm of the output performance signal over the disturbance inputs at the final time T. Hence, the LTV touchdown analysis has to be executed six times, once for each touchdown condition for each wind setup.

Two separate Monte Carlo analyses of the full nonlinear closed-loop are necessary to evaluate the head- and tailwind scenarios' touchdown conditions. Each scenario is evaluated for 10000 samples defined by the parameter set in Tab. 1.

4.2 Results

For the 10kts tailwind scenario, the LTV worst-case analysis delivered a maximum bank angle at touchdown ϕ_{TD} of 11.29deg, a lateral offset to the centerline $y_{\text{LG,TD}}$ of 11.4m, and a worst-case sideslip angle of the landing gear $\beta_{\text{LG,TD}}$ of 17.17deg. The corresponding Monte Carlo analysis identified maximum values of 11.27deg, 8.36m, and 11.13deg for the bank angle, lateral offset, and sideslip angle, respectively. For the 30kts headwind scenario, the LTV worst-case analyses identified 11.01deg for the bank angle, 14.46m for lateral offset, and 17.61deg for the sideslip angle. The corresponding Monte Carlo analysis' results are 10.72deg for the bank angle, 13.42m for the lateral offset, and 16.37deg for the sideslip angle. Thus, each Monte Carlo analysis is upper bounded by the respective LTV worst-case. This is visualized in Fig. 6, showing the two Mont Carlo analyses' histograms and their most critical value and the individual LTV worst-cases. Notably, the six LTV analyses were completed in 46min, which is around seven times faster than the 320min required for the two Monte Carlo simulations, given relatively small sample sizes. Also, there is no general rule on how large the sample size must be to draw conclusions for the design process. Therefore, the LTV analysis is more viable to assess the qualitative impact of design changes rapidly. All analyses were run on a standard desktop computer equipped with Intel i7 processor and 32GB memory. Furthermore, only the LTV worst-case analysis identifies (guaranteed) worst-cases, whereas the Monte Carlo analysis can only

provide lower bounds on the touchdown conditions. Besides, the distribution in Fig. 6 indicates that the latter requires large sample sizes to allow for meaningful conclusions on the most critical touchdown scenarios. In Fig. 7, the most critical y_{LG}

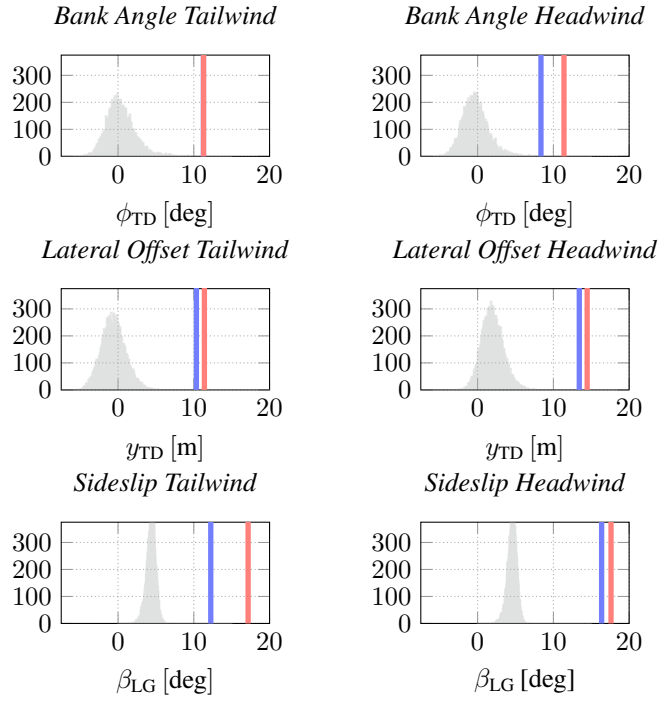

Fig. 6. Analysis Results: LTV worst-case analysis (—), Histogram Monte Carlo simulation (—), Most critical Monte Carlo results(—)

value identified in the Monte Carlo simulations for head- and tailwind are plotted against the corresponding LTV worst-cases. It can be seen that, the LTV worst-case provides a not overly conservative upper bound for the nonlinear simulation.

5. CONCLUSION

The proposed robust LTV analysis of an autolanded aircraft provides fast upper bounds on worst-case touchdown conditions under crosswind. The common LPV aircraft representation is simplified to a special finite horizon LTV case, exposing the autoland scenario's characteristics. This allows to explicitly respect the changing dynamics and control laws under the restriction of the final approach's finiteness. Feasible upper bounds for the Monte Carlo simulations conducted on corresponding high-fidelity nonlinear model are provided by the LTV worst-case analysis in a fraction of time. Thus, the proposed approach delivers a supplemental tool for the design process and evaluation of autoland controllers.

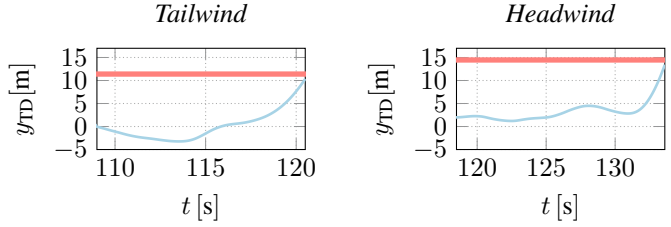

Fig. 7. Comparison of lateral offset from flare initiation to touchdown: Most critical nonlinear Simulation (—), LTV worst-case bound (—)

REFERENCES

Biannic, J.M. and Boada-Bauxell, J. (2017). A civilian aircraft landing challenge. Technical report, ONERA, Toulouse. Online available from the aerospace benchmark section of the SMAC Toolbox, http://w3.onera.fr/smac.

Biannic, J.M. and Roos, C. (2015). Flare control law design via multi-channel H_∞ synthesis: Illustration on a freely available nonlinear aircraft benchmark. In *2015 American Control Conference (ACC)*. IEEE.

Biertümpfel, F. and Pfifer, H. (2018). Worst case gain computation of linear time-varying systems over a finite horizon. In *2nd Conference on Control Technology and Applications*.

Biertümpfel, F. and Pfifer, H. (2019). Finite time horizon worst case analysis of launch vehicles. In *21st IFAC Symposium on Automatic Control in Aerospace*.

Birkle, J.W. (1956). Automatic approach tests of a type d autopilot in a canberra t.4 aircraft at woodbridge airfield, r.a.e. technical note no: Bl.41. techreport 41, UK National Archives DSIR 23/24675.

Boeing (2018). Statistical summary of commercial jet airplanes accidents 1959–2017. Technical report, The Boeing Company, Worldwide Operations, Seattle, Washington,D.C.

Green, M. and Limebeer, D.J.N. (1995). *Linear Robust Control*. Prentice-Hall, Inc., Upper Saddle River, NJ, USA.

Hindi, H., Seong, C.Y., and Boyd, S. (2002). Computing optimal uncertainty models from frequency domain data. In *Proceedings of the 41st IEEE Conference on Decision and Control, 2002*. IEEE.

Iannelli, A., Seiler, P., and Marcos, A. (2019). Worst-case disturbances for time-varying systems with application to flexible aircraft. *Journal of Guidance, Control, and Dynamics*, 42(6), 1261–1271.

Knoblach, A., Pfifer, H., and Seiler, P.J. (2015). Worst case analysis of a saturated gust loads alleviation system. In *AIAA Guidance, Navigation, and Control Conference*. American Institute of Aeronautics and Astronautics.

McRuer, D.T., Graham, D., and Ashkenas, I. (1974). *Aircraft Dynamics and Automatic Control*. Princeton University Press.

Misra, G. and Bai, X. (2020). Updated simulation results of UAV carrier landings. In *AIAA Scitech 2020 Forum*. American Institute of Aeronautics and Astronautics.

Pfifer, H. and Seiler, P. (2016). Less conservative robustness analysis of linear parameter varying systems using integral quadratic constraints. *International Journal of Robust and Nonlinear Control*, 26(16), 3580–3594.

Seiler, P. (2015). Stability analysis with dissipation inequalities and integral quadratic constraints. *IEEE Transactions on Automatic Control*, 60(6), 1704–1709.

Seiler, P., Moore, R.M., Meissen, C., Arcak, M., and Packard, A. (2019). Finite horizon robustness analysis of LTV systems using integral quadratic constraints. *Automatica*, 100, 135–143.

Tadmor, G. (1990). Input/output norms in general linear systems. *International Journal of Control*, 51(4), 911–921.

Theis, J., Ossmann, D., Thielecke, F., and Pfifer, H. (2018). Robust autopilot design for landing a large civil aircraft in crosswind. *Control Engineering Practice*, 76, 54–64.

Veenman, J., Scherer, C.W., and Köroğlu, H. (2016). Robust stability and performance analysis based on integral quadratic constraints. *European Journal of Control*, 31, 1–32.